Effect of Porosity on the Stiffness of Cast Steel

RICHARD A. HARDIN and CHRISTOPH BECKERMANN

The effect of porosity on the elastic behavior of cast steel is investigated experimentally, and an approach for including porosity effects in finite element analysis (FEA) simulations is presented. Porous cast steel specimens are mechanically tested having apparent elastic moduli reduced between 17 and 61 pct. Analysis of radiographs and tomography is used to measure and reconstruct the porosity distribution in these test specimens. The porosity distribution is incorporated into FEA simulations, where elastic mechanical properties are dependent on the locally varying porosity. A relationship between elastic modulus and porosity $E(\phi)$ is determined by minimizing the difference between the simulations and the measurements: $E(\phi) = E_0 (1 - \phi/0.5)^{2.5}$, where E_0 is the elastic modulus of the sound material and ϕ is the porosity volume fraction. It is found that the elastic modulus decreases nonlinearly with porosity and that the steel exhibits a critical porosity level above which it loses all stiffness. This study shows that the stiffness of porous materials depends not only on the amount of porosity, but on how it is distributed and other characteristics such as pore shape and size. By modeling the effect of the porosity distribution in the simulations, the measured strain is predicted within ± 10 pct agreement.

DOI: 10.1007/s11661-007-9390-4

I. INTRODUCTION

TYPICALLY, inhomogeneities in cast metal due to porosity or inclusions are not considered directly in part design. Instead, *ad-hoc* safety factors may be used, which might do little for the robustness of the design other than increasing casting weight. Engineering approaches are in development to consider the effects of porosity on the service performance of cast components.[1,2] As steel castings become lighter weight and thinner sectioned, knowledge of the location, amount, and effect of porosity on strength and fatigue behavior is more critical than ever. When this knowledge is combined with casting process modeling that predicts the location, amount, and size characteristics of micro- and macroporosity, an integrated design process will emerge allowing designers to simulate the possible effects of casting production processing on part service performance.[2] It is anticipated that such a design process will guide and improve inspection criteria as well. In this work, a method for predicting the effects of macroporosity on steel stiffness and modulus of elasticity is presented, and simulations using the method are compared with experimental measurements.

Porosity occurs in natural resources (*e.g.*, wood, bone, coral, and rock) and can form in man-made materials (*e.g.*, concrete, foams, ceramics, composites, and metals). Stiffness and strength properties of porous materials depend not only on the amount of porosity, but on its distribution relative to imposed loads, and on other characteristics such as pore shape and size.[3–7] Ceramics, foams (metallic or polymeric), and sintered metals usually have homogenous and uniformly distributed porosity characterized by volumetric amount, size, and shape of pores, and cellular structure. For homogenous porous materials, the apparent mechanical properties are sufficient for engineering design.[8] Designing components from such materials can be straightforward provided that methods for predicting mechanical properties exist[3] and local variations in the stress-strain field due to the pores can be ignored.

In the case of cast metals, every effort is made to produce a sound, porosity-free casting. Still porosity may occur in a part that is undetectable or that cannot be eliminated without unreasonable cost, making the part "unfriendly" to cast. If it forms, one hopes the porosity will be detectable by nondestructive testing and evaluation (NDT and NDE), but microporosity may form that is difficult to detect. Microporosity may not result in a detectable loss of stiffness, localized stress concentration, or stress redistribution, but it can greatly affect ductility and fatigue resistance.[9,10] Macroporosity, defined here as porosity visible without magnification (typically, >100 μm), can cause gross section loss that reduces the local effective elastic modulus. Stress-strain redistribution occurs in the part due to the macropores, and stress concentrations occur near macropores leading to localized plastic deformation and the development of cracks that cause failure. Finally, macroporosity is not uniformly distributed throughout the part so casting material properties are nonhomogenous.

It has been suggested the stiffness and strength behavior of porous materials can be categorized in

RICHARD A. HARDIN, Research Engineer, and CHRISTOPH BECKERMANN, Professor, are with the Department of Mechanical and Industrial Engineering, University of Iowa, Iowa City, IA 52242, USA. Contact e-mail: becker@engineering.uiowa.edu
Manuscript submitted May 11, 2007.
Article published online November 13, 2007

three classes based on porosity level:[11] (1) less than 10 pct, (2) 10 to 70 pct, and (3) materials having greater than 70 pct porosity. This partitioning is based on the very different appearance and behavior of materials at the two extremes, which are described using models with disparate fundamental assumptions. The wide range in the middle is left over given that assumptions for the models at the two extremes are violated there. Stiffness of materials in the lowest porosity range are described by models with the assumption that voids do not interact,[12] and the strength and plastic behavior can be modeled considering either isolated pores or a uniform distribution of pores.[13,14] A well-known micromechanics-based model is the porous metal plasticity model, describing the plastic behavior of such "mildly voided" materials, that is available in the finite element analysis (FEA) software ABAQUS.[13–15] Materials in the >70 pct porosity range are typically cellular or foam materials, and physical models of these materials are developed using representative volumes having strutlike edges of solid material in the case of open-cell "sponge" materials or membrane-walled cells in the case of closed-cell "honeycomb" materials.[3,16,17] The physical nature of highly porous cellular materials is quite different from what is observed in porosity in steel castings, where an ordered homogeneous and isotropic distribution of porosity is not found throughout the cast part.

When the assumptions in the lowest porosity range are violated and pores begin to interact and cause stress redistribution, the level of porosity is in the intermediate range. In the intermediate porosity regime of noncellular materials, a fundamental behavior not observed in cellular materials occurs when a critical porosity fraction ϕ_0 is reached. Above this porosity level, there is no longer an interconnected solid throughout the volume of material, and the material looses all stiffness and load carrying capability. The elastic modulus becomes zero. An additional ramification is that ϕ_0 is the largest porosity level where a uniform/homogenous porosity distribution can exist in a representative elemental volume. The critical porosity fraction has been experimentally and empirically observed[7,11,18,19] and demonstrated through analytical and computational modeling.[5–7,20,21] Based on empirical observation, Bert[19] suggested such behavior for porous materials, where the elastic modulus E depended on porosity ϕ according to

$$E(\phi) = E_0 \left(1 - \frac{\phi}{\phi_0}\right)^n \qquad [1]$$

and $E(\phi) = 0$ if $\phi > \phi_0$. In Eq. [1], E_0 is the elastic modulus of the sound material, n is a power exponent that has been found to vary in measurements between 0.5 and 4 (typically $n > 1$), and ϕ_0 is the critical porosity fraction ranging from 0.37 to 0.97.[6,7] In general, n and ϕ_0 depend on the pore shape and size on a microscopic scale.

The general behavior of Eq. [1] is demonstrated in Figure 1. When $\phi_0 = 1$, it behaves as the linear rule-of-mixtures equation for $n = 1$ (curve) and appears as a power exponent decaying to $\phi_0 = 1$ when $n = 2.5$. When $\phi_0 < 1$, such as $\phi_0 = 0.5$ in the case of the lower two curves in Figure 1, the apparent modulus is noticeably reduced from the cases where $\phi_0 = 1$. This is clear by comparing the curves for $\phi_0 = 1$ and $\phi_0 = 0.5$, with $n = 2.5$ for both. The critical porosity fraction has a great effect. Comparing the two lowermost curves for $n = 2.5$ and 4, with $\phi_0 = 0.5$ for both as indicated on the abscissa axis of Figure 1, illustrates the effect of increasing the power exponent in reducing the apparent modulus still further.

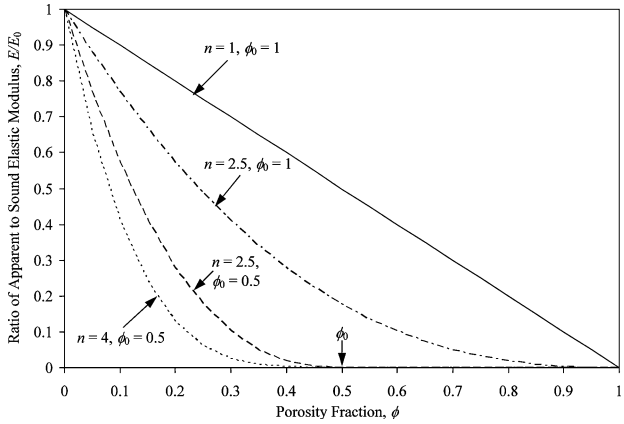

Fig. 1—Curves resulting from Eq. [1] for values of $n = 1$, 2.5, and 4 and $\phi_0 = 1$ and 0.5.

Experimental data in the reviewed literature show how n and ϕ_0 depend on pore shape and other characteristics of the pores on a microscopic scale.[5–7,21] Rice[21] analytically demonstrated for packed beds of spheres and cylinders in various stacking arrangements that the minimum solid area fraction of contact (MSA) in the packing is an excellent predictor of the relative properties of the porous structures. Furthermore, ϕ_0 is shown to be the porosity fraction where the MSA in the packing asymptotically approaches zero. In analytical studies using the MSA concepts, ϕ_0 is found to range from 0.26 to 1.0 depending on the packing shape and arrangement.[7] When a normalized porosity ϕ/ϕ_0 is used to plot the results, the MSA fraction *vs* ϕ/ϕ_0 for all geometries and arrangements of porous structures collapse to a narrow band of curves.[7] Measurements and analyses both give physical credibility to Eq. [1] and demonstrate the importance of identifying ϕ_0 for porous structures.

Computer simulations of elastic and plastic properties of materials add additional credence to using Eq. [1] and the MSA concepts. Roberts and Garboczi[6] developed computer generated representative elemental volumes of porous structures having porosity fractions up to 0.5 made up of three fundamental geometries: overlapping solid spheres, overlapping spherical pores, and overlapping ellipsoidal pores. Geometric bodies in the structures were randomly sized, positioned, and oriented in the case of the ellipsoids, to achieve a porosity fraction. The solid material (having elastic properties E_0 and Poisson ratio ν_0) with interstitial spaces was meshed and analyzed using FEA. It was found that the relative elastic modulus E/E_0 of the structures depended as much on porosity type or shape as it did on the porosity

fraction; at the same porosity fraction, E/E_0 varied substantially, from 0.25 to 0.46 at $\phi = 0.3$, for example. The structure made from overlapping solid spheres was found to have the greatest reduction in elastic modulus with increasing porosity, where Eq. [1] and $n = 2.23$ and $\phi_0 = 0.652$ gave an excellent fit to the simulated E/E_0. Herakovich and Baxter[5] predict the elastic and plastic properties of Al_2O_3 for idealized pore shapes (cylinder, cube, sphere, and cross-shaped) using the generalized method of cells (GMC). It is shown[5] that pore geometry is as important as pore volume fraction to E for a porous structure, because the elastic modulus of the porous material can vary by up to 2 times for different pore shapes at the same porosity volume fraction. Experimental measurements for sintered porous metals also follow the behavior of Eq. [1], where E/E_0 is less than 0.05 for $\phi > 0.3$ for porous copper,[11] and $E/E_0 \approx 0.1$ at $\phi = 0.35$ and $E/E_0 \approx 0$ at $\phi = 0.7$ for porous titanium.[22]

In the present study, measurements are used to develop a relationship between elastic modulus and porosity. This $E(\phi)$ relation is applied to an arbitrary porosity distribution, producing a variation in E that is used in FEA predicting the elastic response of axially loaded 8630 cast steel test specimens. Radiographic and tomographic analysis of porosity in the test specimens are performed along with mechanical testing. From radiographs taken of the specimens before testing, image analysis is used to measure the porosity distribution within the specimens. From this, it is shown that the volumetric average porosity in the gage section of axial test specimens is an insufficient indicator of the measured effective stiffness of steel containing porosity. It is concluded that the effective elastic modulus depends on how the porosity within the gage section is distributed, and not just on the average amount. X-ray tomography is used to reconstruct the porosity distribution. This porosity distribution is mapped onto a finite element mesh so the mechanical testing can be realistically simulated. Given the past success using Eq. [1] to describe the effect of porosity on apparent elastic modulus E of material with porosity, property data of E vs ϕ is generated using Eq. [1]. The data are then used in the simulations to determine the parameters n and ϕ_0, which give the best overall agreement between predicted and measured strain for test specimens made from cast 8630 steel.

II. PROCEDURES

A. *Cast Specimens and Mechanical Testing*

As-cast blanks were designed using computer modeling[2,10] to produce a range of shrinkage porosity levels. The as-cast blanks were 152 mm long cylinders having a nominal 14.3 mm diameter. To produce a hot spot at the midlength of the castings, a cylindrical disk 25.5 mm in diameter was positioned at the midlength of the as-cast specimen. The severity of the hot spot, and resulting porosity, was manipulated by changing the disk thickness (dimension along the casting length); disk thicknesses of 5, 7.5, and 10 mm were cast to provide a range of porosity levels. Generally, a smaller disk thickness resulted in a lower porosity level, but there was an overlap of the volumetric average porosity level between the three disk thickness groups. Cut-surfaces of specimens from castings having disk thicknesses of 5, 7.5, and 10 mm are shown in Figures 2(a), (b), and (c), respectively. One can see that the porosity level ranges between dispersed macroporosity, to holes, and gross section loss. Radiographs are shown to the right of each cut specimen surface with a white mark indicating the approximate location of the cut along the length of the machined specimen. Comparing the entire radiographs, a qualitative evaluation can be made that the porosity appears to be increasingly severe proceeding from Figures 2(a), to (b), and to (c).

The design of the as-cast blanks concentrated porosity at the centerline and midlength of the castings so that the porosity was located in the gage section of the test specimens. Specimens were machined to the dimensions shown in Figure 3(a). It was found that the as-cast blanks could be machined without visible macroporosity on the specimen surface when viewed without magnification, but on closer inspection using 5 times magnification, discontinuities from the porosity at the surface could be observed in some specimens. The cast steel composition was AISI 8630, and the material was quenched and tempered. Additional production details of the cast steel specimens and testing are given elsewhere.[10] The test specimen design, preparation, and fatigue testing were performed according to the ASTM E606 standard.[23] Results of the fatigue testing are given in Reference 10, and the present work will deal only with the elastic property recorded during the fatigue testing.

During fatigue testing the mechanical behavior of the specimens was found to be elastic, so load-controlled testing at 10 to 20 Hz was used. This allowed for accurate strain amplitude measurements while using the faster testing capability of load control. An extensometer with ends at 6 mm above and below the midpoint of the specimen length was used to measure strain amplitude. The effective (or apparent) elastic modulus E was determined from the extensometer and load data, using the ''sound'' specimen gage section area A_0 and load to determine the nominal stress and the strain from the extensometer. The measurements for the 25 specimens analyzed in this article are given in Table I. Reference will be made to individual specimens in the table using the specimen numbers. Four nominal stress levels σ_a were applied and held constant during testing of the specimens; 126, 96, 66, and 53 MPa. The applied load, combined with the individual porosity distribution in a given specimen, resulted in a range of measured modulus of elasticity E and fatigue life data.[10] The range of loads also randomized any systematic errors of the effect of applied load on measuring E. In many cases, larger strains were measured in specimens at lower stress levels due to more severe porosity present. The measured modulus of elasticity E was determined from the stable cycle hysteresis loop data for the unloading portion of the loop by taking the average of the data for a large

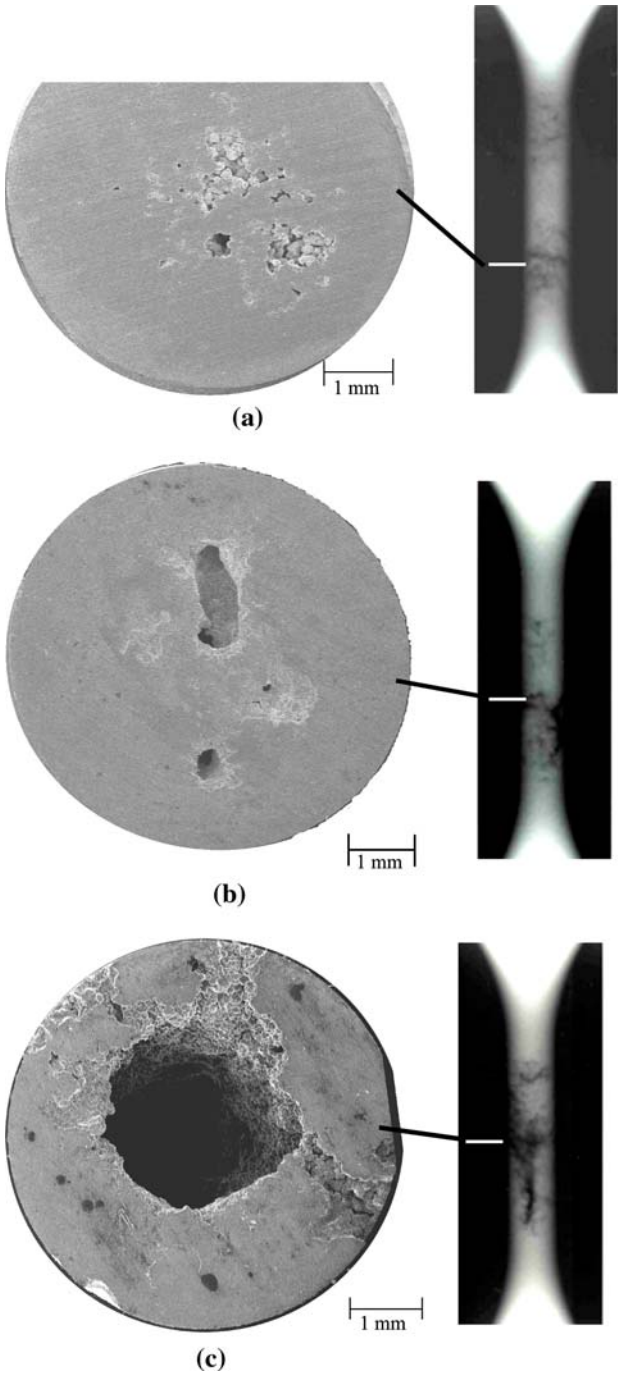

Fig. 2—Cut and polished surfaces of three specimens cast with different porosity levels ranging from (*a*) specimen 22 representing the least, to (*b*) specimen 3 representing the middle range, to (*c*) specimen 13 representing the most porosity. Radiographs of the specimen gage sections are given to the right of each surface with the longitudinal position of the cut indicated.

number of cycles. The elastic modulus of 8630 steel without porosity E_0 is taken to be 207 GPa, as measured from keel block data.[24] From the measured modulus of elasticity E, an effective specimen area A_e was calculated from $A_e = A_0 \frac{E}{E_0}$. The effective specimen area A_e is the cross-sectional area that a completely sound specimen (with E_0) would have in order to produce the measured

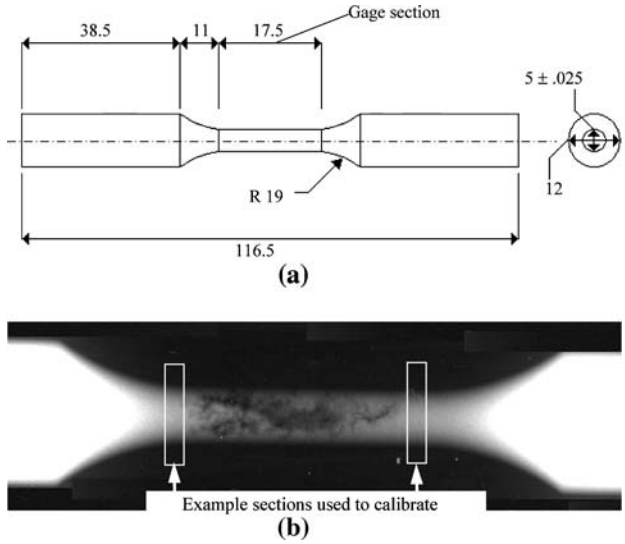

Fig. 3—(*a*) Dimensions of test specimens in millimeters. (*b*) Radiograph of test specimen with sections of sound material used to calibrate gray level intensity to section thickness indicated.

strain for the applied test force. The difference between the nominal section area A_0 and A_e could be thought of as an effective porosity area A_{pore}.

B. *Radiographic Measurement, Analysis, and Tomography*

Film radiography of the fatigue test specimens was performed at Alloy Weld Inspection Co. (Bensenville, IL) using a sensitivity of 2 pct of the gage section diameter (100 μm). Two orthogonal radiographic views of each specimen were shot using marks and a 90 deg gage angle to align the specimens. The film radiographs were digitized using an X-ray scanner resulting in 8-bit gray level, 1200 dpi images. An example radiograph is shown in Figure 3(b). Quantitative analysis of the radiographs was performed using *ImageJ* to extract gray level and coordinate position data from the radiographs, and software written by the authors to perform the analysis and computed tomography. The radiographs were used to measure and reconstruct the porosity in the test specimen gage sections. Indications on radiographs are typically thought of as "point density" indications and are directly related here to the thickness of the material. The gray level intensity on the radiographs depends primarily on the total thickness (or effective density) of material through which the X-ray passes, if scattering and spreading of the X-rays is negligible. An *in-situ* gray level *vs* steel thickness calibration was performed for each radiograph image analyzed using sound selections of the specimen gage sections, such as those indicated in Figure 3(b). Because the cross section of steel through which the X-rays pass is circular, the X-ray paths trace parallel chords of the circle for each radiographic view. The thickness of steel corresponding to these chord lengths is known from the coordinate position data in the planar view of the specimen. The centerline of the specimen is used as the

Table I. Experimental Measurements and Average Simulation Results: Test Stress Level, Porosity Measurement from Radiographic Analysis, Predicted and Measured Strain and Elastic Modulus

Specimen Number	Applied Stress Level σ_a (MPa)	Porosity Fraction		Strain $\varepsilon \cdot 10^4$		Elastic Modulus E (GPa)	
		Average in Gage Section	Maximum Cross section	Measured	Predicted Average	Measured	Predicted Average
1	96	0.104	0.432	7.01	8.08	137	119
2	96	0.101	0.208	6.44	7.31	149	131
3	126	0.101	0.256	8.81	9.29	143	136
4	53	0.128	0.297	3.84	4.36	138	121
5	126	0.097	0.185	8.24	7.37	153	171
6	66	0.134	0.275	4.55	5.78	145	114
7	66	0.095	0.201	4.68	4.48	141	147
8	66	0.185	0.363	4.89	5.78	135	114
9	53	0.146	0.587	6.09	6.80	87	78
10	126	0.213	0.326	9.33	8.67	135	145
11	66	0.117	0.250	4.85	4.08	136	162
12	66	0.148	0.415	5.84	4.38	113	151
13	96	0.185	0.538	12.47	12.36	77	78
14	126	0.139	0.507	10.50	13.60	120	93
15	53	0.187	0.551	6.09	7.47	87	71
16	66	0.076	0.160	3.98	3.67	166	180
17	96	0.096	0.254	8.65	9.86	111	97
18	53	0.085	0.148	3.66	3.44	145	154
19	126	0.093	0.225	8.87	8.31	142	152
20	53	0.099	0.182	3.71	3.80	143	140
21	96	0.122	0.300	7.68	6.90	125	139
22	66	0.117	0.262	4.37	4.81	151	137
23	126	0.121	0.205	8.13	8.86	155	142
24	96	0.144	0.288	6.76	8.94	142	107
25	126	0.129	0.280	8.51	12.73	148	99

position reference where the maximum steel thickness is the gage section diameter. Moving radially outward from the centerline, additional gray level *vs* thickness calibration data is generated. Performing this calibration for each radiograph removes the uncertainties of image-to-image variability due to the original X-ray and scanning processes. In this study, radiographic analysis and tomography are performed in the specimen gage section only.

Once a calibration curve for the radiograph gray level *vs* steel thickness for a specimen's image is determined, a mapping between the coordinates on the radiograph and the known, or nominal, specimen geometry is performed. From the specimen geometry, the thickness of steel can be calculated at any point in the radiograph, assuming the specimen is entirely sound. Finally, a calculation of the cumulative steel thickness absent at any point in the radiograph due to porosity can be made by taking the difference between *what the thickness would be if sound* (from the sound geometry to radiograph mapping) and *what the thickness actually is* (from the radiograph gray level and the calibration curve). In terms of a quantitative porosity measure at a given point in a radiographic view, the total porosity along the X-ray path is the ratio between the steel thickness determined to be missing due to porosity and the thickness at that point if the specimen were sound. Because the calibration process is performed for each specimen image, the uncertainty and accuracy of each measurement varies; typically the accuracy of the method to determine total material loss due to porosity is no worse than 300 μm (6 pct of the gage section diameter) based on the calibration errors and repeatability of the process. However, for two specimens' sectioned surfaces investigated under a scanning electron microscope, the authors have found by measuring total porosity dimensions that the method is capable of identifying individual features as small as 200 μm (4 pct of the gage section diameter) and determining cumulative material absent due to porosity of the same resolution.

Digitized radiographs for two orthogonal radiographic views of specimen 3 are provided in Figure 4. At any position along the specimen length, the section thickness from the radiographic analysis can be summed across the specimen diameter to determine the cross-sectional area present in the specimen. Also, by subtracting this from the specimen's nominal section area, the porosity area in a longitudinal section can be determined. The porosity fraction (and percentage) in a longitudinal section area is determined from the ratio of porosity area to nominal section area. The darker indications in Figure 4 denote steel that is less dense, having greater total void dimension in the specimen, as shown by the scale provided. The longitudinal position of the maximum cross-sectional porosity percentage at +3.2 mm above the midlength of the specimen is indicated for both views in Figures 4(a) and 4(b). A plot of the cross-sectional porosity variation along the specimen length is shown in Figure 5 for the two views shown in Figures 4(a) and 4(b). The cross-sectional porosity data for these two views agree with each other quite well in Figure 5, and appear to have a relatively

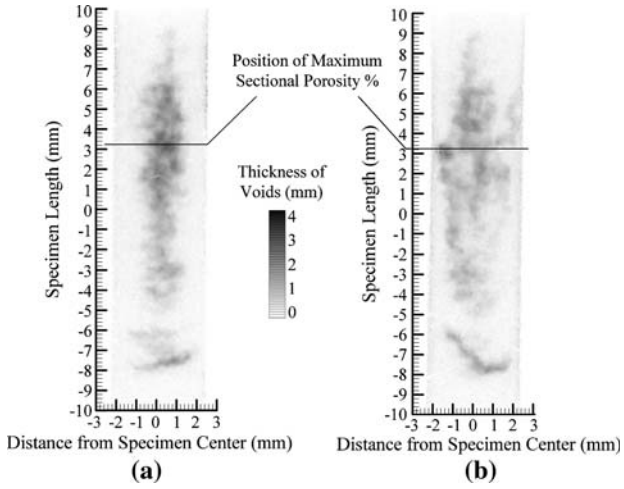

Fig. 4—(*a*) Digitized radiograph of specimen 3, view 1. (*b*) Second radiographic view of same specimen taken after rotating 90 deg about lengthwise axis, view 2.

constant offset bias error. There is an excellent correspondence between the longitudinal positions of the maximum cross-sectional porosity in the two views. A horizontal line on the ordinate axis at 5.4 mm^2 in Figure 5 indicates the effective porosity area determined from the measured modulus for this specimen, $A_{pore} = A_0 - A_e$. Good agreement is observed between the maximum value of the section porosity area from the radiographic analysis and A_{pore} from the measured modulus. On the other hand, the horizontal line on the ordinate axis at ~2 mm^2, indicating the average porosity area over the entire gage length does not agree with A_{pore} from the measured modulus. These findings for specimen 3 are generalized to all specimens later in the section of this article containing the results of the analysis of the radiographs.

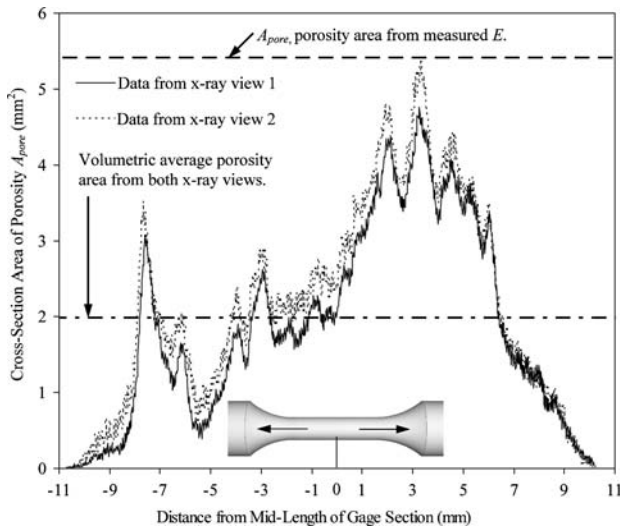

Fig. 5—Cross-sectional area of porosity *vs* lengthwise axis position of specimen 3, position referenced to center of specimen length for the two radiographic views that were shown in Fig. 4. Volumetric average porosity and effective porosity area determined from measured modulus are indicated for comparison.

Tomography was required to take the analysis further and to reconstruct a realistic three-dimensional porosity field within the specimens so that they could be simulated using FEA. A tomography algorithm was developed based on algebraic reconstruction principles.[26] In the method, a Cartesian grid formed by the X-ray paths of the two orthogonal radiographic views is created over the cross section of the specimen at lengthwise positions. The dimensions of the grid in the cross section and the length increments are defined by the pixel dimensions in the digitized radiograph (1200 dpi or ~21 μm side length). This defines the voxels in which porosity is reconstructed. In each cross-sectional plane, the porosity is determined such that the error between the total void dimension of porosity determined from the radiograph and the total void dimension resulting from the tomographic reconstruction is minimized for both views. The algorithm is iterative and marches by cross section along the specimen length determining the porosity field. At a given lengthwise position, iterations begin by assuming that a uniform level of porosity produces the total void dimension indicated by the first radiographic view. Next, porosity values in the voxels aligned with the second radiographic view (along X-ray traces orthogonal to the first) are summed to determine a total porosity dimension for this view. After summing, the total dimension is compared with the actual value from the second view, and all values of porosity in the summation are corrected so the total void dimensions agree. Returning to the first view the summation process is repeated; summation along X-ray trace paths followed by a correction to achieve agreement between the total porosity dimensions from the radiograph and that from the summation of voxel porosity values. Typically, about 30 iterations between the two views are required to achieve a minimized error. From the tomography, a three-dimensional field of porosity data is determined for the cylindrical specimen gage section, which can be mapped to the nodal locations of a finite element mesh. Elastic mechanical properties are then defined as a function of porosity, and the elastic behavior of each specimen can be simulated using porosity dependent properties that vary locally with its porosity field.

C. *Simulation Procedures*

Mechanical simulation of the specimens with porosity was performed using the commercial FEA package ABAQUS/Standard[27] to determine n and ϕ_0 in Eq. [1], which give the best agreement between the predicted and measured strain for all specimens. This required simulations with spatially varying elastic properties that depend on the local porosity volume fraction ϕ. For this purpose, the measured tomographic porosity field of a specimen was mapped onto the FEA mesh. It is beyond the scope of the present study to directly resolve the geometry of the pores on a microscopic scale in the FEA simulations. This would require a FEA mesh (and a tomographic reconstruction) with a resolution of the order of 1 μm over a specimen gage length of approximately 20 mm, which is not possible given present-day

computing resources. Instead, a porosity volume fraction ϕ is defined for a representative elemental volume that is large compared to the pore microstructure but much smaller than the specimen itself. Recall from Section I that the effect of the microscopic pore geometry is accounted for by Eq. [1] in an average sense. Thus, the FEA node spacings used in the present study were chosen to be between one and two orders of magnitude larger than the size of the voxels in the tomographic porosity reconstruction (~21 μm), that is, between 200 μm and 2 mm. Such FEA node spacings are large enough to allow for a meaningful calculation of porosity volume fractions from the tomographic data, but small enough to resolve variations in the porosity over the entire specimen volume (*e.g.*, Figure 5). A detailed investigation of the sensitivity of the simulation results to the choice of the node spacing is presented in Section III.

In order to determine the sensitivity of the simulation results to the method used to map the porosity distribution from the tomography onto the FEA mesh nodes, two methods were tested to perform the necessary interpolation. One method used the three-dimensional quadratic interpolation subroutine QD3VL from the IMSL Math Library to map the porosity from the tomography data onto the FEA mesh.[28] The second method was developed by the authors and took the average of a cubic volume of tomography porosity data centered at a FEA mesh node with the side dimensions of the cube determined by the neighbor node spacing. Ten-node quadratic tetrahedral elements were used to perform the stress/displacement analysis. The sensitivity of the simulation results to the method of porosity mapping is discussed further in Section III.

The elastic material properties used in the FEA analysis are made dependent on the porosity by defining porosity as a predefined field variable in ABAQUS. For given values of n and ϕ_0, Eq. [1] was used to generate elastic modulus data as a function of porosity fraction. Because this study deals only with elastic behavior, the only material property of concern other than E is the Poisson ratio ν. Porosity affects the Poisson ratio for porous materials. However, this dependency does not appear to have a large effect on the overall effective elastic modulus.[6] In light of this, it was determined that a relationship from Roberts and Garboczi[6] should be used for the dependence of ν on ϕ:

$$\nu(\phi) = \nu_S + \frac{\phi}{\phi_\infty}(\nu_\infty - \nu_S) \qquad [2]$$

with $\nu_\infty = 0.14$, $\phi_\infty = 0.472$, and $\nu_S = 0.3$. This is the result for an overlapping solid spherical geometry porosity distribution. Because there was not significant plasticity detected during testing of the specimens, plastic effects were ignored in the FEA simulations used to develop the best E *vs* ϕ relationship.

The FEA simulation boundary conditions were prescribed to closely match the test conditions. During testing, specimens were held fixed at their upper grip, and the loading was applied to the lower (ram) end, which was free to move vertically placing the specimen in tension and compression during fatigue testing. The simulated specimen geometry considered only the initial 5 mm of the length of the grips in the FEA mesh. This was a more than sufficient distance away from the fillet and test section to produce stress-strain results, which were insensitive to where the boundary and loading conditions were applied. The only difference from simulations using more of the grip length was longer execution times. At the upper grip face, a clamped boundary condition was applied (having no translations or rotations), and at the lower grip, translations were allowed only in the axial direction with no axial rotation allowed. A uniform distributed loading was applied over the face at the lower grip end to produce the total load corresponding to the testing conditions.

Because the specimens had nonuniform properties in the gage section, a nonuniform stress-strain field occurred during testing. The strain varied about the circumference of the specimen in the test section where the extensometer was located. Unfortunately, it was not possible to measure this complex strain distribution on the specimen surface. Also, because the circumferential orientation of the gage was not recorded, a closer comparison with the simulated strain at the appropriate circumferential position could not be made. It was assumed that the strain measured was the average strain at the extensometer. Predicted strains were determined from the FEA simulations using the relative displacements at axially aligned locations on the surface of the specimen FEA model where the extensometer was placed in testing. The extensometer was placed with its ends at 6 mm above and 6 mm below the midlength of the specimen gage section. Therefore, the predicted strain was determined from the axial displacements at ± 6 mm, about the midlength of the gage section on the surface of the ABAQUS FEA mesh. The solid model and mesh were partitioned such that groups of nodes were always located at the extensometer edges so that the predicted strain was determined from the simulation displacements at node circumferential positions, 12 mm apart, centered in the gage section. An average strain was determined from these values, and a 95 pct confidence interval was determined to provide an indication of uncertainty for this average, which reflects the circumferential variability in predicted strain on the specimen surface.

III. RESULTS

A. *Results from Analysis of Radiographs*

An example of the analysis of the two radiographic views is provided in Figure 5, showing the variation in porosity section area along a specimen's gage length. Here, the maximum cross-sectional porosity area along the gage length corresponds well with A_{pore} derived from the measured E. The overall agreement between these two porosity areas is borne out in Figure 6(a) by the good linear correspondence between E and the maximum value of the cross-sectional porosity fraction from the radiographic analysis of all specimens. Results in

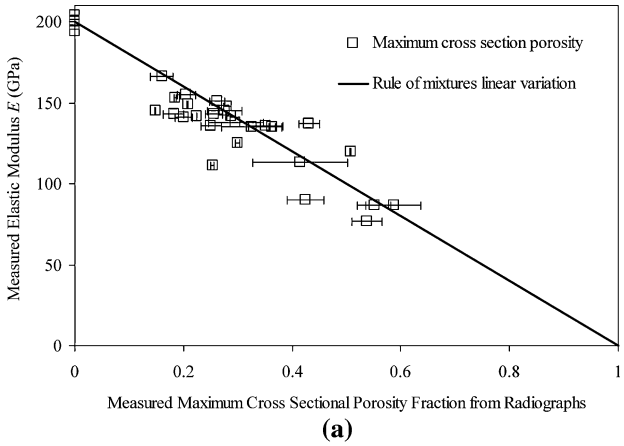

Fig. 6—(*a*) Measured elastic modulus *vs* maximum section porosity for all radiographic views (two per specimen) plotted at error bars with mean at symbol. Plot includes sound specimen data as well to emphasize linearity back to no porosity. (*b*) Average porosity.

Figure 6(a) are given for both radiograph views; there are two abscissa values per specimen represented as error bars while the symbol is the mean value. Sound test data taken during the study, having $E \approx 200$ GPa, are included in the plot to show that the data appears to follow the rule-of-mixtures behavior for a solid phase mixed with a pore phase having $E = 0$, which is the line extending from $E = 200$ GPa at $\phi = 0$ to $E = 0$ at $\phi = 1$. Also note this line corresponds to Eq. [1] with $n = 1$ and $\phi_0 = 1$. Unfortunately, the good correlation observed in Figure 6(a) cannot be used to analyze the elastic response of castings having porosity and complex loadings. For such multiaxial stress situations, it would be difficult to define and translate the information in Figure 6(a) for such cases. For instance, how does one determine the maximum sectional area of porosity for an arbitrary distribution of porosity and multiaxial stress field? Nonetheless, Figure 6(a) is remarkable. It is consistent with the MSA models and concepts proposed by Rice,[21] because the measurement of the maximum value of the section porosity is an indicator of the minimum solid area fraction of contact (MSA).

The radiographic analysis in Figure 5 shows that the average cross-sectional porosity area over the entire specimen gage length compares poorly with A_{pore} derived from the measured E. The data in Figure 5 can be summed over the entire gage section volume and averaged to determine the volumetric average porosity in the specimen gage length. A plot of the measured elastic modulus E for all specimens *vs* this volumetric average porosity is shown in Figure 6(b). Here, the volumetric average porosity in the gage section is shown to be a poor indicator of the measured effective stiffness, because for all data, E varies by more than a factor of 2 even though the volumetric average porosity in the gage section is scattered between 8 and 22 pct. In particular, consider the two data points circled, specimens 9 and 24. They each have an average pore fraction of about 0.145. Yet, "24" has $E = 142$ GPa and "9" has $E = 87$ GPa. These two specimens will be compared later in the article in more detail, because they clearly show the importance of porosity distribution in addition to porosity amount on effective elastic behavior.

B. *Results of Tomography*

From the two X-ray views of each specimen, a three-dimensional porosity field is reconstructed such that at each position along the specimen length, the distribution of total void thickness across the specimen diameter for the two X-ray views agrees with those determined from the reconstructed distribution. This concept is illustrated in Figure 7, where the total void dimensions from the tomography distribution are compared with measurements from the radiographic analysis at one position along the length of a specimen. As shown in Figures 7(a) and 7(b), the tomography provides a reconstructed porosity field having dimensional characteristics that agree very well with the porosity void dimensions measured in the two radiographic views across the specimen diameter at an arbitrary lengthwise position. These results are typical for any lengthwise position, and essentially represent the converged solution for the tomography algorithm at one lengthwise position.

Comparisons between cross sections of the reconstructed porosity field and selected cut/polished sections of specimen surfaces examined under a scanning electron microscope assisted the determination of parameters used in the algebraic reconstruction algorithm. For instance, the minimum value of porosity allowed in a voxel was 5 pct, based on detectability limits and the ability to resolve the interfaces of larger cavities, as shown in Figure 8 for specimen 22. Here, the tomographic distribution is compared with an image of the cut surface from the specimen at the same lengthwise position examined after mechanical testing. The porosity amount and features of the reconstructed field compare well with the cut section considering only two X-ray views were used. Figure 8 shows the three-dimensional nature of the distributions generated by the tomography technique via the iso-surfaces of porosity $\phi = 0.75$ distributed along the specimen length. The tomography results were found to be a good representation of the porosity field for the purposes of this study. Certainly, using more radiographic views and additional algorithm development will improve the fidelity of the

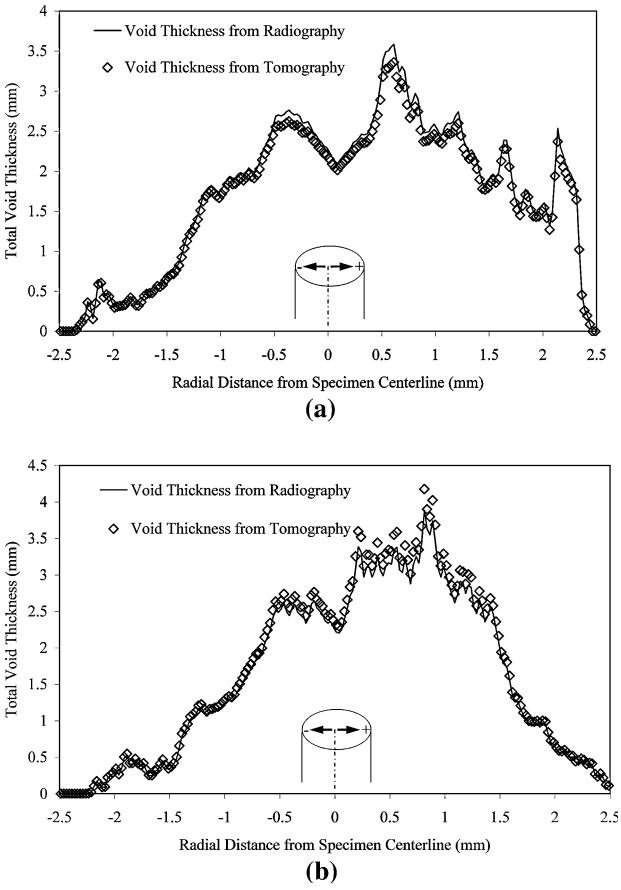

Fig. 7—Comparison between the total void dimension of the porosity determined from the radiograph and resulting from the tomographic reconstruction of the porosity for two radiographic views (*a*) and (*b*). Data are from a lengthwise position in the specimen gage section across the specimen diameter.

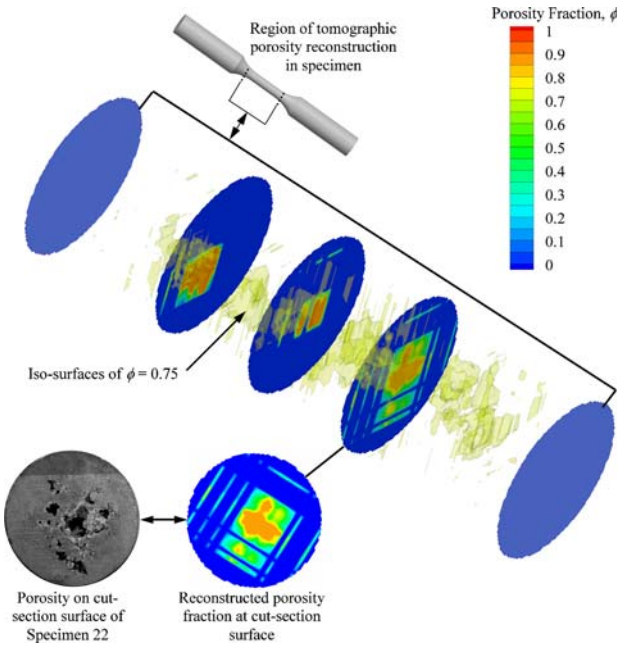

Fig. 8—Example of internal porosity distribution reconstructed from X-ray tomography in the test section of a fatigue test specimen, specimen 22. Slice of the three-dimensional porosity field from tomography is compared to a cut specimen surface at the same lengthwise position.

reconstruction. Even so, results from this tomography algorithm were adequate for quantitative comparative analysis of the differences in porosity distributions, and their effect on the effective stiffness in these specimens. Note also that the very high resolution porosity field is interpolated onto a much coarser finite element mesh when the tomography results are put to use.

C. *Simulation Results*

The porosity distribution is mapped onto the nodes of a FEA mesh. Figures 9(a) and 9(b) are provided as an example of this mapping for one specimen. In Figure 9(a), the output of a porosity distribution from tomography is shown, which is then mapped onto the finite element mesh in Figure 9(b). To assist in visualizing the effect of the mapping on the detailed reconstructed porosity, iso-surfaces of porosity $\phi = 0.5$ are shown. Here, the tomography results are determined on a three-dimensional grid defined by the 1200 dpi resolution from the digital radiographs. The FEA mesh is approximately 20 to 50 times coarser than this. Two issues affecting this mapping were investigated: (1) how the interpolation of the tomography ϕ field onto the mesh influences the FEA results, and (2) how the coarseness of the mesh influences the FEA results.

Two methods of performing the interpolation between the tomography porosity distribution and the finite element mesh were tested. As shown in Figure 10(a) on a nodal mesh spacing of 1 mm for specimen 13, one method used a three-dimensional quadratic interpolation scheme to map the porosity in the tomography data to the FEA mesh. The second method took the average of a cubic volume of tomography porosity data centered at a node with the side dimension of the cube determined by the node spacing. The averaged cubic volume method shown in Figure 10(b) resulted in a more diffuse representation of the porosity. The differences between the two interpolated porosity distributions shown in Figures 10(a) and (b) are subtle, especially if one compares the porosity distribution for a finer mesh shown in Figure 11(a) for the same specimen. On a fine mesh, such as those shown in Figures 11(a) and 11(b), no difference was observed in the fields resulting from the two interpolation methods, which should be expected. The FEA simulation results for the two porosity interpolation methods were compared on several meshes to look at the effects of grid coarseness, and determine the best combination of interpolation and grid refinement to use in the simulation runs that follow. Three small images set into Figure 11(c) illustrate some of the FEA meshes used in the specimen gage section in the grid dependence study. The three images represent meshes for the node spacings of 1, 0.5, and 0.3 mm.

The effect of grid refinement and interpolation method was investigated using porosity distributions from two specimens identified for grid dependence test

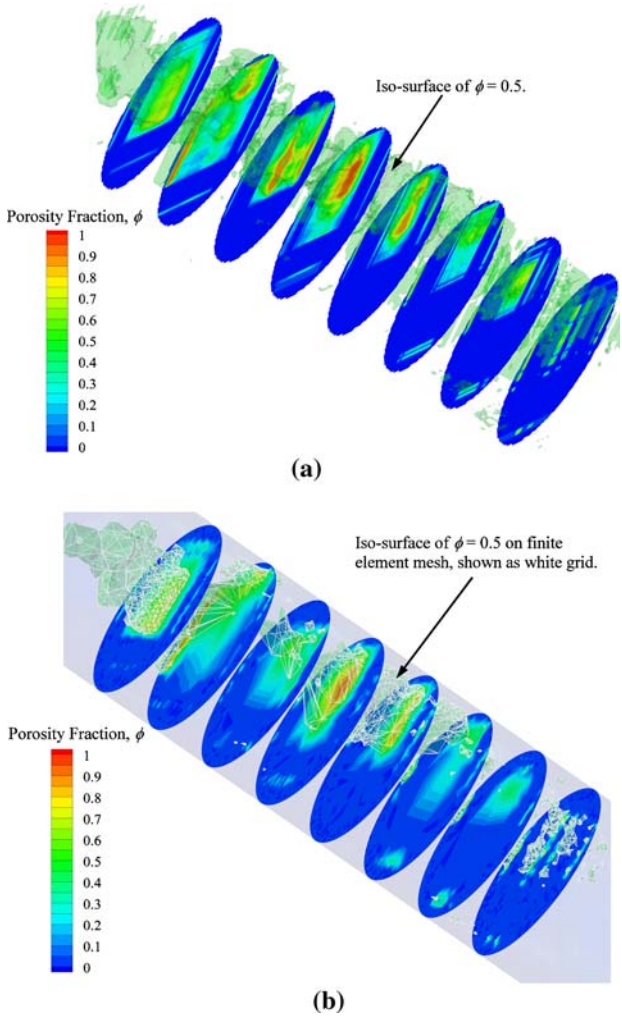

Fig. 9—(*a*) Porosity distribution from tomography showing iso-surface of $\phi = 0.5$ for specimen 25. (*b*) Porosity distribution from mapping tomography results onto the finite element mesh. Same slices of data shown in (a) and (b) with internal structure of FEA mesh shown on $\phi = 0.5$ iso-surface to reflect grid in (b).

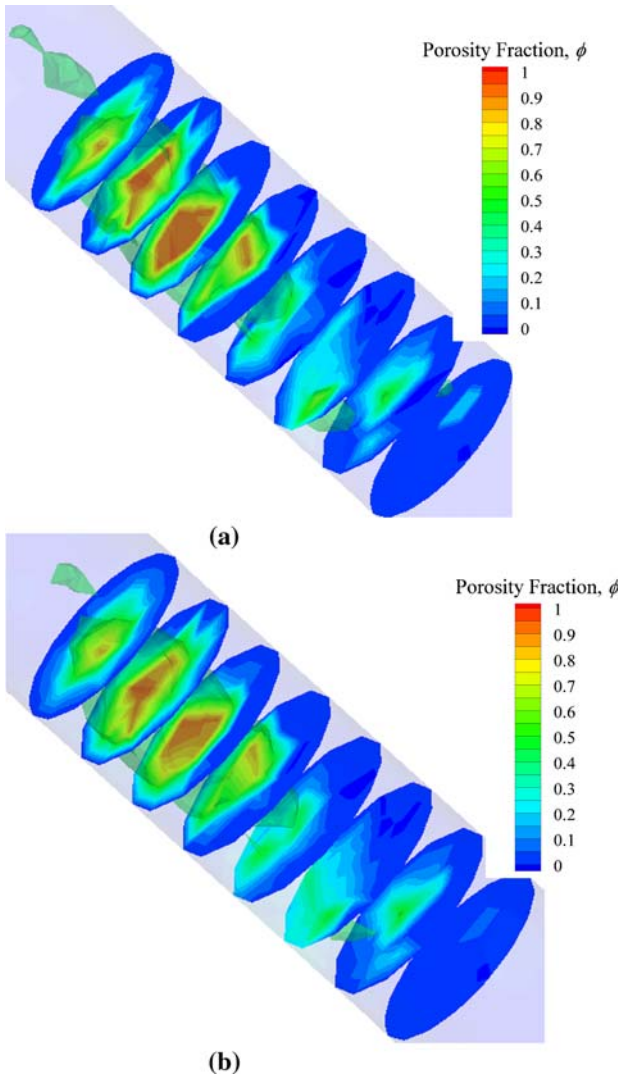

Fig. 10—Longitudinal slices of the porosity distribution for specimen 13 mapped to a FEA mesh having a 1-mm node spacing in the gage section. Mapping interpolation performed using (*a*) a three-dimensional quadratic interpolation method and (*b*) an average value from a cubic volume around the mesh nodes.

cases. Specimens 13 and 1 were chosen for this. Specimen 13 was selected because it was found to have the most reduced elastic modulus. Specimen 1 was chosen because it was tested at the same stress level (96 MPa) as ''13'' but had a marked difference in porosity severity, as seen in Figures 11(a) and 11(b). Specimens were held fixed at their upper grip, and the lower (ram) end was pulled and was free to displace; these boundary conditions were used in the finite element modeling also. The ram end displacement was selected as the variable monitored in the grid dependence studies, because it appeared to be the most sensitive single simulation output to changes in the grid and porosity field. Shown in Figure 11(c), the ram end displacement of the more porous specimen 13 is about 33 pct larger than the less porous specimen 1. Results for specimen 1 do not reflect much variation with either grid spacing or interpolation method. The specimen 13 ram end displacement shows that the average volumetric interpolation monotonically converges with finer grids, while the quadratic interpolation displacements do not. Recall that the specimen test/gage section diameter was 5 mm. The displacement for the 1-mm spacing is farther away from the finer mesh values, and the 2-mm mesh is closer to the finer meshes. This result points out a drawback in the quadratic interpolation scheme; on coarser meshes, it is more influenced by values near the node than desirable, and results can oscillate for coarser meshes. Despite this drawback, it was decided to use the quadratic interpolation scheme on a 0.5-mm mesh spacing, because this mesh and interpolation scheme will guarantee capture of fine detail in the porosity distribution and have reasonable simulation run times. Probably, either interpolation method would have worked just as well for the 0.5-mm mesh spacing, which was used in subsequent simulations to determine the best E *vs* ϕ relationship. For the 0.5-mm node spacing, the simulation mesh consisted of 39,119 elements and

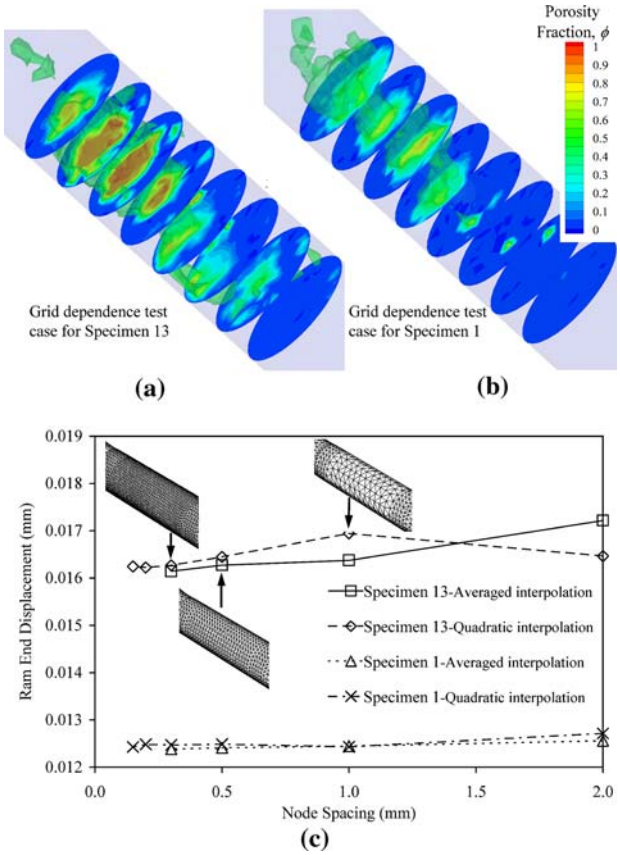

Fig. 11—Porosity distributions at the 0.5-mm node spacing for (*a*) specimen 13 and (*b*) specimen 1. (*c*) Grid dependence study results for lower grip end displacement *vs* FEA mesh node spacing for two interpolation methods. Both specimens were tested at the same nominal stress level σ_a = 96 MPa.

57,651 nodes, and execution run times ranged from approximately 1 to 3 hours on a workstation with dual AMD Opteron 252 2.6 GHz processors. It was observed that more severe porosity distributions resulted in longer run times due to an increase in solver iterations and smaller solution increments.

Because it had the most severely reduced E, specimen 13 was chosen as the starting point for the FEA simulations to develop the E *vs* ϕ relationship that would give the best agreement with the measurements. Comparison between measured and predicted strain would be used to determine the best E *vs* ϕ relation. The nonuniform porosity for specimen 13 was shown earlier in Figure 11(a) and is shown at a center longitudinal cut in Figure 12(a). The predicted stress-strain fields have variations throughout the porous region in the specimen gage section caused by the nonuniform stiffness. The stress and strain fields for a simulation using E data from Eq. [1] with n = 2.5 and ϕ_0 = 0.5 are shown in Figure 12(b) and 12(c), respectively. The nominal sound gage section stress for this test was 96 MPa.

To compare the FEA results with the measurements, axial displacements at ±6 mm about the center of the gage section on the surface of the FEA mesh were used to determine the predicted strain. As can be seen in Figure 13 for specimen 13, the strain variations at the

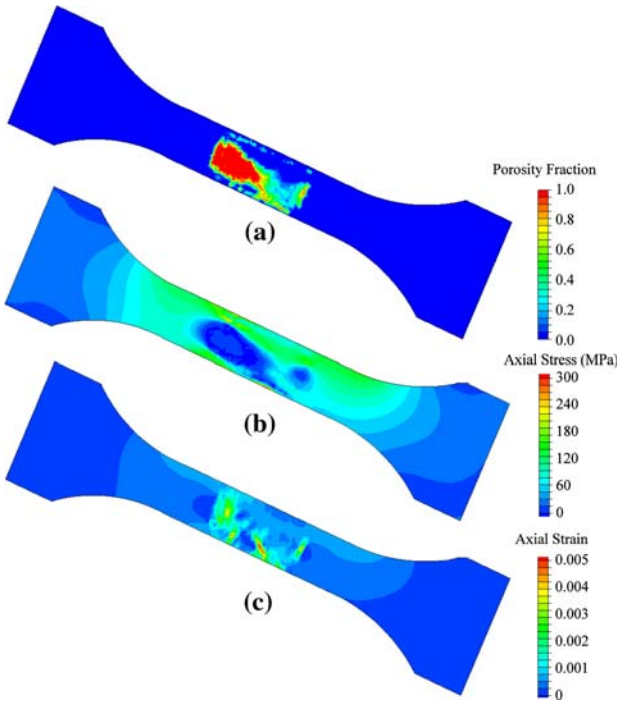

Fig. 12—Centered longitudinal section of ABAQUS simulation results for specimen 13: (*a*) porosity fraction, (*b*) axial stress, and (*c*) axial strain. Nominal gage section stress is 96 MPa based on a porosity-free gage section.

surface of the specimen are predicted to vary from 200 to 600 microstrain. Recall that the predicted strain is determined by averaging at the extensometer location and providing an estimate of the variation around the specimen circumference using the 95 pct confidence interval of these data. Results of strain predictions using Eq. [1] with ϕ_0 = 1.0 and variable n for specimen 13 are compared with the measured strain in Figure 14. Here, the exponent n was chosen to cover the range of n values observed in the literature, from 1 to 5. As n increases, E is reduced progressively and the average predicted strain increases along with the variation in

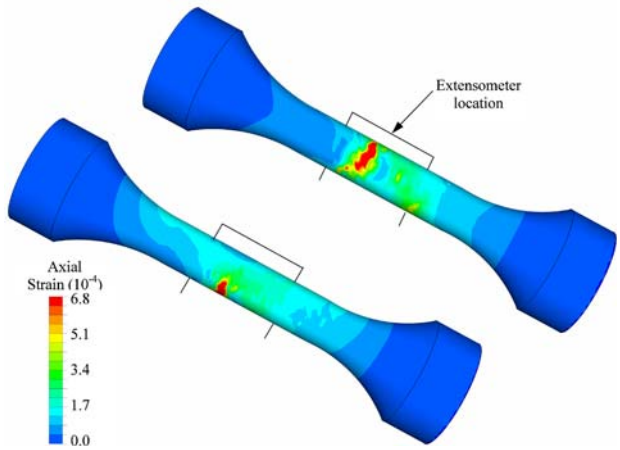

Fig. 13—Variation in axial strain on the surface of specimen 13. Two rotated views show axial strain on surface in gage section varying from 200 to over 680 microstrain.

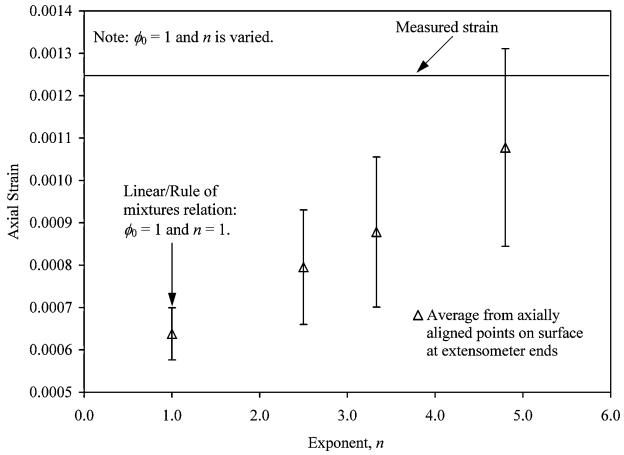

Fig. 14—Effect of n on results of strain predictions compared with the measured strain using Eq. [1] with $\phi_0 = 1.0$ and variable n for specimen 13 shown in Fig. 13. Error bars indicate ±1 standard deviation.

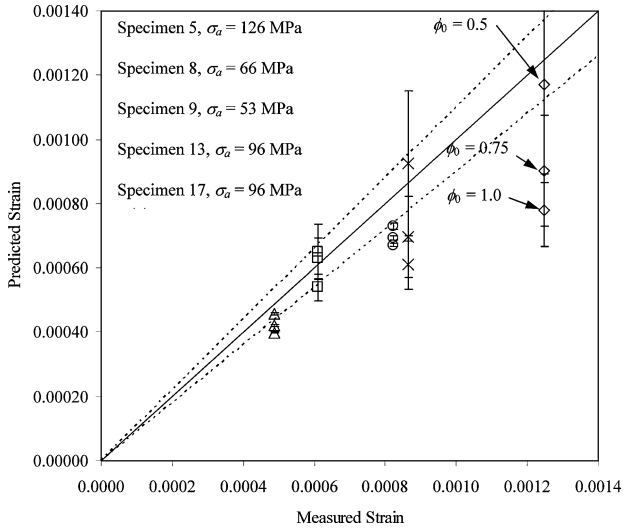

Fig. 15—Effect of critical porosity fraction ϕ_0 on predicted *vs* measured strain for five test case specimens using elastic modulus *vs* porosity relation Eq. [1] with $n = 2.25$, and critical porosity fraction $\phi_0 = 1.0$, 0.75, and 0.5. Increasing predicted strain occurs with decreasing ϕ_0 as indicated for test case 13. Applied nominal stress σ_a given for each test case.

strain reflected by the confidence interval. When $n = 1$ (the linear relation), the strain is underpredicted by about 50 pct. Only as n is increased to 5 (a very high value and just outside the range of data in the literature) does it approach the measured strain. Here, the effect of critical porosity is not considered, $\phi_0 = 1.0$. For $\phi_0 = 1.0$, results for all specimens simulated were found to greatly underpredict the strain for reasonable values of n. This was a strong indication that steel with porosity has a critical porosity fraction ϕ_0 less than 1.0.

Taking guidance from Roberts and Garboczi,[6] the effect of critical porosity fraction ϕ_0 was investigated with a fixed exponent of $n = 2.25$ in Eq. [1]. Five test case specimens were chosen because they encompassed the full range of porosity levels and nominal test stresses. Of these, specimen 13 was discussed earlier, and the remaining four are specimens 5, 8, 9, and 17. The specimens were chosen to cover the range of applied nominal stress and porosity levels for comparison. The results are shown in Figure 15 with critical porosity fractions $\phi_0 = 1.0$, 0.75, and 0.5 used to generate variable stiffness properties in the FEA simulations. For each specimen, the predicted strain increases progressively as ϕ_0 decreases; this is indicated in Figure 15 for specimen 13 at the far right in the plot. The applied nominal stress level is also indicated for each specimen in Figure 15. Note that specimen 5 was tested at the highest nominal stress level, 126 MPa, but is only in the middle strain range of the specimens shown here. The predicted strain of specimen 5 is not influenced much by the different critical porosity fractions ϕ_0 because it is one of the more sound specimens tested. specimen 8 is relatively sound and was tested at a lower stress level (66 MPa); its predicted strain is uninfluenced by changing ϕ_0. Results for specimen 9 show a discernable variation in strain even though it was tested at the lowest stress level (53 MPa); it had a low measured E so that is not too surprising. Overall, the results in Figure 15 indicate the following: (1) ϕ_0 has a nonlinear effect on the strain prediction, and (2) $\phi_0 = 0.5$ provides good agreement for the range of specimens analyzed in Figure 15. The nonlinear behavior of the specimens in response to changing ϕ_0 is driven by the porosity distribution in the specimens.

The best-fit values for the parameters n and ϕ_0 in the E vs ϕ relation were determined by minimizing the error between the predicted and measured strain for all specimens available. This was accomplished by a trial and error procedure: (1) generating the elastic modulus *vs* porosity data according to Eq. [1] for a given n and ϕ_0, (2) importing that data in a format usable by ABAQUS to define the material properties dependent on a field variable, (3) running ABAQUS simulations for the applied nominal stress conditions for specimens with the mapped porosity field and porosity dependent E and ν, and (4) comparing the measured and predicted strain and determining how to change n and ϕ_0 to get better agreement. Good overall agreement between the measured and predicted strain was obtained using Eq. [1] with $n = 2.5$ and a critical porosity fraction of $\phi_0 = 0.5$, which is shown in Figure 16. Comparison of the n and ϕ_0 from this work with the most reduced E property results from Roberts and Garboczi[6] show our n value to be slightly higher ($n = 2.5$ *vs* 2.23) and our ϕ_0 somewhat lower ($\phi_0 = 0.5$ *vs* 0.652). This basic agreement instills some confidence in the present results, especially because the analysis of the specimens is complicated by the fact that the porosity distributions are inhomogeneous, as opposed to the uniform porosity in the representative elementary volumes studied by Roberts and Garboczi.[6] As discussed earlier, the values established here for n and ϕ_0 reflect in an average sense the effect of the size and shape of the shrinkage pores, on a microscopic scale, on the stiffness of a representative elementary volume of cast steel with a porosity amount equal to ϕ. These values could be refined further, but

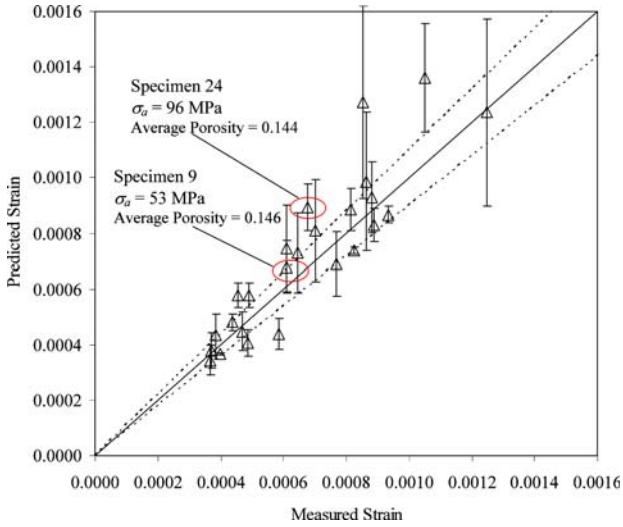

Fig. 16—Predicted strain from FEA simulations *vs* measured strain with simulations using E as function of porosity from Eq. [1] with $n = 2.5$, and critical porosity fraction $\phi_0 = 0.5$. Line of perfect correspondence and ±10 pct band also plotted.

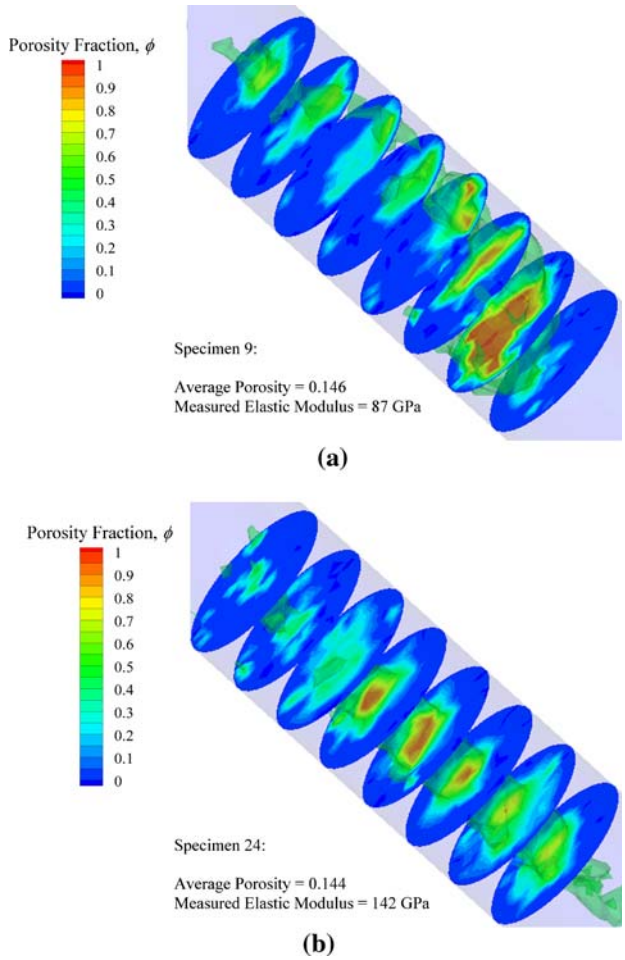

Fig. 17—Porosity distributions in slices along the gage section in two specimens having the same average porosity and measured E differing by about 40 pct.

more accurate tomography and strain measurements that would give the variation in strain about the specimen surface would be needed.

The importance of accounting for the macroscopic distribution of the porosity in the specimens is further illustrated by examining the two specimens identified in Figure 6(b). They are identified again in Figure 16, specimens 9 and 24. Considering their porosity distributions shown in Figure 17(a) and 17(b), the two specimens have nearly identical average porosity levels in the gage section (porosity fractions of 0.146 and 0.144), but the mechanical testing gave very different effective elastic moduli (87 and 142 GPa, respectively). There is not a great difference between the strains for the two specimens (Figure 16), but specimen 9 was tested at a nominal stress level of 53 MPa and specimen 24 at 96 MPa. The porosity in "9" appears to be quite severe in one slice/region along its axis as shown in Figure 17(a), and this feature of the porosity distribution appears to greatly affect the resulting behavior. Comparing the predicted and measured strains, it should be evident that simulations with the correct accounting for the effects of the variations in the porosity in the specimens can explain the material behavior that was obscured in Figure 6(b), where the same average porosity resulted in a nearly twofold range of E. Predicted and measured strain data for all specimens are provided in Table I.

The results of the predicted strain ε_p were converted to a predicted effective elastic modulus E_p of a specimen by using the test's nominal stress:

$$E_p = \frac{\sigma_a}{\varepsilon_p} \qquad [3]$$

where σ_a is the applied nominal test stress and ε_p is the predicted strain. The predicted and measured effective elastic moduli are plotted in Figure 18 and given in Table I. Unfortunately, because of the variation in strain on the specimens' surfaces, and the sensitivity of E_p to ε_p in Eq. [3], the error bars representing the variation in E_p are substantial for many specimens, but the mean values form a good trend of agreement. It is emphasized again that no direct correlation exists between the effective elastic modulus of a specimen and the average porosity in the gage section (as shown in Figure 6(b)). In order to predict the effective elastic modulus it is necessary to account for the variation of the porosity volume fraction in the specimens. As shown in the present study, this can be accomplished by performing a finite element simulation where the porosity field is mapped onto the FEA mesh and the sound elastic modulus is locally degraded according to Eq. [1]. It is clear that the same approach would be needed in analyzing the effect of porosity on the mechanical performance of a complex steel casting.

IV. CONCLUSIONS

As presented in Table I, the porous test specimens examined here had apparent elastic moduli ranging from

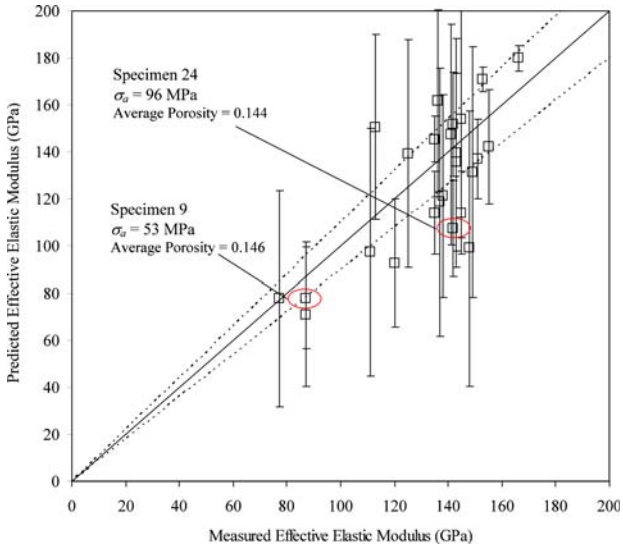

Fig. 18—Predicted *vs* measured elastic modulus with two specimens shown in Fig. 17 indicated. Line of perfect correspondence and ±10 pct band also plotted.

77 to 166 GPa. Because sound steel tested at the same time[10] had $E \approx 200$ GPa, the apparent elastic moduli were reduced between 17 and 61 pct. Radiographic analysis was performed showing an excellent correlation between the maximum cross-sectional porosity fraction and the E measurement, which appears to follow the rule of mixtures. However, the measured elastic modulus does not correlate with the volumetric average porosity determined from the radiographs, which can be attributed to large variations of the porosity in the specimens. To predict the stiffness response of the inhomogeneous specimens, a relationship between elastic modulus and porosity is required that can be applied locally and generally. A tomography algorithm based on algebraic reconstruction principles was developed to determine the distribution of porosity in a specimen so it could be simulated and an E *vs* ϕ relationship established.

Mapping the tomographic porosity distribution onto FEA mesh nodes, stress/strain simulations of the mechanical tests were performed where the elastic properties were locally degraded according to the porosity amount present. Comparing the measured and predicted strain for all specimens, the following relationship for E *vs* ϕ was found to give good overall agreement: $E(\phi) = E_0 (1 - \phi/0.5)^{2.5}$. This equation demonstrates that E decreases nonlinearly with porosity fraction. The values of 0.5 and 2.5 were determined by minimizing the difference between the measured and predicted strain. They reflect the average effect of the pore geometry (*i.e.*, shape and size) on a microscopic scale. In particular, the value of 0.5 represents a critical porosity level above which the material essentially looses all stiffness or load carrying capability. A thorough review of the literature on the properties of various kinds of porous materials supports the basic form of this relation and these values. Therefore, it is reasonable to assume that the present E *vs* ϕ relationship also applies to shrinkage porosity in cast materials other than steel.

The stiffness behavior of steel with porosity can be accurately modeled by incorporating the present relationship for the elastic modulus as a function of porosity into finite element simulations, and this should result in accurate stress-strain fields in the elastic regime. The result is a major advance from past work in the area because it considers a nonuniform distribution of porosity, such as that found in steel castings, and demonstrates that inhomogeneities due to porosity can be considered in FEA. The method can be extended to analyses of the performance of steel parts and their design. The effect of porosity in redistributing stress and strain, and increasing their magnitudes, in complex components and force loadings can be effectively modeled using this relationship. The present approach should be useful in such analyses especially because the grid sensitivity study showed that accurate results are obtained even for relatively large FEA node spacings. Because tomographic reconstruction of porosity fields is quite cumbersome, it is envisioned that the porosity volume fraction distribution in a casting can instead be obtained from advanced solidification simulation software.

Improvements could be made, in particular to improve the fidelity of the porosity reconstruction and to reduce the uncertainties in the measurements. The X-ray tomography reconstruction used here is relatively crude and approximate considering the highly advanced state-of-the-art. By having a more realistic porosity field, one would have greater faith in the simulation's realism, but it is difficult to see whether that would have much of an impact on the fundamental findings. A side-by-side comparison of the simple tomographic method used here with more advanced methods could be made to determine whether this is worth pursuing. The extensometer used to sense the strain measurements presented here could be replaced by a strain gage or several gages carefully positioned and mapped to compare with simulations. Recording the variability of strain on the specimen surface through measurement or visualization would have also added much to this work.

ACKNOWLEDGMENTS

This research was undertaken through the American Metalcasting Consortium (AMC). The AMC is sponsored by Defense Supply Center Philadelphia (DSC, Philadelphia, PA) and the Defense Logistics Agency (DLA, Ft. Belvoir, VA). This work was conducted under the auspices of the Steel Founders' Society of America (SFSA) through substantial in-kind support and guidance from SFSA member foundries. Any opinions, findings, conclusions, or recommendations expressed herein are those of the authors and do not necessarily reflect the views of DSC, DLA, or the SFSA and any of its members.

REFERENCES

1. M.F. Horstemeyer, R.J. Osborne, and D.E. Penrod: *AFS Trans.*, 2002, vols. 02–036, pp. 1–18.
2. R.A. Hardin, R.K. Huff, and C. Beckermann: in *Modeling of Casting, Welding and Advanced Solidification Processes—XI*, C. Gandin and M. Bellet, eds., TMS, Warrendale, PA, 2006, pp. 653–60.
3. L.J. Gibson and M.F. Ashby: *Cellular Solids: Structure and Properties*, 2nd ed., Pergamon Press, Oxford, United Kingdom, 1997.
4. N. Ramakrishnan and V.S. Arunachalam: *J. Am. Ceram. Soc.*, 1993, vol. 76 (11), pp. 2745–52.
5. C.T. Herakovich and S.C. Baxter: *J. Mater. Sci.*, 1999, vol. 34, pp. 1595–1609.
6. A.P. Roberts and E.J. Garboczi: *J. Am. Ceram. Soc.*, 2000, vol. 83, pp. 3041–48.
7. R.W. Rice: *J. Mater. Sci.*, 2005, vol. 40, pp. 983–89.
8. M.F. Ashby, A.G. Evans, N.A. Fleck, L.J. Gibson, J.W. Hutchinson, and H.N.G Wadley: *Metal Foams: A Design Guide*, Butterworth-Heinemann, Boston, MA, 2000.
9. P. Heuler, C. Berger, and J. Motz: *Fatigue Fract. Eng. Mater. Struct.*, 1992, vol. 16 (1), pp. 115–36.
10. K.M. Sigl, R. Hardin, R.I. Stephens, and C. Beckermann: *Int. J. Cast Met. Res.*, 2004, vol. 17 (3), pp. 130–46.
11. E. Zhang and B. Wang: *Int. J. Mech. Sci.*, 2005, vol. 47, pp. 744–56.
12. J.M. Dewey: *J. Appl. Phys.*, 1947, vol. 18, pp. 578–81.
13. A.L. Gurson: *J. Eng. Mater. Technol.*, 1977, vol. 99, pp. 2–15.
14. V. Tvergaard: *Int. J. Fract. Mech.*, 1981, vol. 17, pp. 389–407.
15. *ABAQUS Theory Manual*, Version 6.5, Hibbit, Pawtucket, RI, Karlsson and Sorensen, Inc., 2004.
16. S.K. Maiti, L.J. Gibson, and M.F. Ashby: *Acta Metall.*, 1984, pp. 1963–75.
17. L.J. Gibson and M.F. Ashby: *Proc. R. Soc. London, Ser. A*, 1982, vol. 382, pp. 43–59.
18. R.L. Coble and W.D. Kingery: *J. Am. Ceram. Soc.*, 1956, vol. 39 (11), pp. 377–85.
19. C.W. Bert: *J. Mater. Sci.*, 1985, vol. 20, pp. 2220–24.
20. R.W. Rice: *J. Am. Ceram. Soc.*, 1995, vol. 76 (7), pp. 1801–08.
21. R.W. Rice: *J. Mater. Sci.*, 1996, vol. 31, pp. 102–18.
22. C.E. Wen: *J. Mater. Sci.-Mater. Med.*, 2002, vol. 13, pp. 397–401.
23. American Society of Testing and Materials: *2002 Annual Book of ASTM Standards*, ASTM, West Conshohocken, PA, 2002, vol. 03.01, pp. 569–83.
24. R.I. Stephens: *Fatigue and Fracture Toughness of Five Carbon or Low Alloy Cast Steels at Room or Low Climatic Temperature*, Steel Founders' Society of America, Des Plaines, IL, 1982.
25. W. Rasband: *ImageJ 1.35p*, National Institutes of Health, Bethesda, MD.
26. A.C. Kak and M. Slaney: *Principles of Computerized Tomographic Imaging*, Society for Industrial and Applied Mathematics, Philadelphia, PA, 2001, pp. 275–96.
27. *ABAQUS/Standard*, ABAQUS, Inc., Providence, RI, 2006.
28. *IMSL Fortran Subroutines for Mathematical Applications: Math/Library Volumes 1 and 2*, Visual Numerics, Inc., 1997.